Nuclear Inst. and Methods in Physics Research, A 1010 (2021) 165558

Contents lists available at ScienceDirect

Nuclear Inst. and Methods in Physics Research, A

journal homepage: www.elsevier.com/locate/nima

# New design of a magnetic device for wide-angle XYZ polarization analysis PASTIS-3, from the concept to first tests with thermal neutrons

David Jullien *, Alexandre Petoukhov, Mechthild Enderle, Nicolas Thiery, Pascal Mouveau, Ursula Bengaard Hansen, Philippe Chevalier, Pierre Courtois

*Institut Laue-Langevin, 71 Avenue des Martyrs, CS20156, 38042 Grenoble Cedex 9, France*

ARTICLE INFO

*Keywords:*
Polarized neutrons
$^3$He neutron spin-filter
Polarization analysis
Neutron instrumentation

ABSTRACT

We present the new concept and neutron test results of the third generation PASTIS device for XYZ wide-angle polarization analysis for thermal neutrons. PASTIS-3 uses two polarized $^3$He Neutron Spin filter Cells (NSF) for polarizing and analyzing neutrons spins, flipping the incident neutron beam polarization by reversing the $^3$He spin state of the polarizing entrance cell. We detail a new coil design for high spatial homogeneity of the magnetic field in any field direction, and the calculation method employed to optimize the geometry and to characterize the field gradients. Various components of the apparatus are described with particular attention to their performance and impact on the relaxation time of the NSF cells. Finally, we present test results of the new device tested on the thermal triple-axis spectrometer IN20 at the ILL.

## 1. Introduction

XYZ polarization analysis of polarized neutrons (PA) is a powerful method for the separation of magnetic, and nuclear coherent and incoherent scattering, particularly adapted for neutron instruments equipped with wide-angle detectors [1]. For this technique, the neutron polarization is adiabatically transported to the sample in a selected direction (e.g. X, Y, Z), and the scattered beam is spin-analyzed along the same direction as the polarization of the incident beam. This analysis can be performed for a large range of scattering angles. For thermal neutrons, a polarized $^3$He neutron spin-filter (NSF) that is placed close to the sample is the most attractive solution as a wide-angle spin-analyzer. While supermirror devices can also be considered for wide-angle analysis [2], they suffer from low angular acceptance at short wavelengths and the rapid variation of the spin-dependent reflectivity as a function of the incident angle onto the supermirror. In contrast, the efficiency of a $^3$He NSF filter with silicon windows has a well-known wavelength dependence, the dependence of the scattering angle and the beam divergence are negligible, which makes them ideally suited for thermal and hot neutrons.

The first wide-angle device for XYZ Polarization Analysis on Thermal Inelastic Spectrometers, also widely known as PASTIS [3], was built at the ILL shortly after the polarized $^3$He NSF technique reached the practical level [4] with a regular supply of spin-filters to instruments. In the PASTIS device, the polarization of the wide-angle NSF was kept by a weak (~1 mT) "Holding" magnetic field of high spatial homogeneity (relative gradients $< 10^{-3}$ cm$^{-1}$) [5]. The required magnetic field was created in X, Y, or Z direction by three pairs of compensated Helmholtz coils. The first version of PASTIS confirmed the feasibility of the complete XYZ analysis based on $^3$He NSF. However, the adiabatic transport and the spin-control of the incident polarized neutron beam were difficult to achieve for all 3 directions of the magnetic field. This simple solution also suffered considerably from blind angles in the scattering planes created by the finite thickness of the coils and their radiological shielding.

A second magnetic device, PASTIS-2 [6], was developed to open the access to horizontal scattering angles over 135° without any blind angles. The magnetic field in the vertical direction was supplied by a Helmholtz coil pair while in X and Y direction it was generated by a pair of quasi-infinite DC-sheets wrapped around thin flat mu-metal cores. The field inhomogeneity was then measured with a 3D field-mapping robot, and the measured field map was employed in subsequent simulations to design adapted correction coils. A total of 22 correction coils were integrated and the correction currents optimized via parallel resistors. The field tuning was complex, dependent on the field direction, the coil current and the (Mezei) flipper state. A further improvement integrated an Adiabatic Fast Passage (AFP) neutron flipper [7–9], this was successfully tested [10] with the Flatcone multi-analyzer of the thermal 3-axis instrument IN20 [11]. An overall spin relaxation time constant of the order of $T_1$~100 h was demonstrated for a banana-shaped analyzer cell ($R_{inner}$~6 cm, $R_{outer}$~12 cm, height 5 cm) with polarized $^3$He at 2 bar pressure. The AFP neutron flipper shows more than 0.99 efficiency in a broad range of thermal energies

* Corresponding author.
*E-mail address:* djullien@ill.fr (D. Jullien).

https://doi.org/10.1016/j.nima.2021.165558
Received 10 November 2020; Received in revised form 3 June 2021; Accepted 4 June 2021
Available online 9 June 2021

independent of the field direction on the sample ($f_{exp}$~0.998 for $k_i = 3$ $A^{-1}$).

Worldwide there are presently several devices of PASTIS type employed on existing instruments or being developed for future instruments with their geometry adapted to the beam characteristics [10,12–17].

In this paper, we present the third generation of magnetic devices, PASTIS-3, which takes advantage from the experience accumulated during the development and exploitation of the previous versions PASTIS and PASTIS-2. It consist of an "iron-free" magnetic insert and hosts two independent polarized $^3$He NSF cells [12], one to polarize the incident beam and the second to allow the wide-angle (130 degrees) XYZ spin-analysis of the scattered beam. We present the concept of the PASTIS-3 device, the optimization of the magnetic system, and details of its components. Finally, we demonstrate the operation of the setup installed on the IN20 spectrometer. We concentrate on the technical aspects of the device. The procedure of the data acquisition and treatment will be published in a separate paper.

## 2. Spin-relaxation processes in NSF cells

As the polarized $^3$He nuclei are far away from thermal equilibrium, the $^3$He polarization decreases exponentially with a time constant $T_1$ which is a decisive criterion for practical applicability, since it conditions the performances of the $^3$He NSF cells over time and how often they have to be changed during an experiment:

$$P_{He} = P_0 e^{-t/T_1} \tag{1}$$

Three effects cause relaxation: dipole–dipole interaction during inter-atomic collisions ($\Gamma_d$) [18], collisions with the container walls ($\Gamma_w$) [19] and the gradients of the magnetic field that applied to define and keep the direction of the spin-filter polarization ($\Gamma_m$). This leads to an overall relaxation rate $\Gamma$:

$$1/T_1 \equiv \Gamma = \Gamma_d + \Gamma_w + \Gamma_m \tag{2}$$

The nuclear-spin-relaxation rate of gaseous $^3$He due to the magnetic-dipole interaction between the $^3$He nuclear spins $\Gamma_d$ was theoretically analyzed in [18]. For $^3$He gas at room temperature (23 °C), the authors give the following estimate of the relaxation rate:

$$\Gamma_d = \frac{817}{p} \tag{3}$$

Here $\Gamma_d$ is given in $h^{-1}$ and p is the gas pressure in bar. Typically, the spin-relaxation due to inter-atomic collisions is important for $^3$He gas at high-pressure (p > 2 bar).

The mechanisms of surface-induced relaxation of nuclear spins remain relatively obscure [20–22]. The relaxation rate $\Gamma_w$ due to interaction with the container walls is cell dependent and difficult to control. Early in the history of polarized $^3$He spin-filters, the container wall relaxation was dominant ($T_w$ ~10 – 50 h) and a lot of effort was invested to improve the relaxation time of polarized $^3$He cells. Today, Cesium or Rubidium coated cells with $T_w$ of the order of a few hundred hours are common.

The spin-relaxation due to inhomogeneity of the magnetic field $\Gamma_m$ was studied in detail in Refs. [5,23,24]. The authors consider the influence of the magnetic field inhomogeneity on the Brownian motion of a spin that leads to a stochastic time-dependent perturbation of the polarized nucleus in its own frame of rest. The following remarkably simple and widely quoted formula for the longitudinal spin-relaxation rate was derived for a magnetic field with the main component directed along $Z$-axis, and small position-independent gradient:

$$\Gamma_m = D\frac{\|\nabla B_x\|^2 + \|\nabla B_y\|^2}{\|B\|^2}, \tag{4}$$

here D is the diffusion coefficient for spin-polarized gas.

A generalization for magnetic fields with an arbitrary spatial inhomogeneity and a gas container of arbitrary form was developed in [25]. In the "adiabatic diffusive regime of motion", where the condition $\omega_0\tau_c \gg 1$ is fulfilled ($\omega_0 = \gamma B$ is the Larmor frequency and $\tau_c$ is the correlation time, or the time required to diffuse through the region where the magnetic inhomogeneity is important), expression (4) is replaced by its volume-averaged value:

$$\Gamma_m = D\left\langle \frac{\|\nabla B_x(\boldsymbol{x})\|^2 + \|\nabla B_y(\boldsymbol{x})\|^2}{\|\boldsymbol{B}(\boldsymbol{x})\|^2} \right\rangle_V \tag{5}$$

Replacing D by its value $D = D_0/p$ , with $D_0 = 7029$ $cm^2$ $h^{-1}$ (at T = 300 K and p = 1 bar [26]), allows to write the more practical expression at room temperature:

$$\Gamma_m \approx \frac{7000}{p}\left\langle \frac{\|\nabla B_x(\boldsymbol{x})\|^2 + \|\nabla B_y(\boldsymbol{x})\|^2}{\|\boldsymbol{B}(\boldsymbol{x})\|^2} \right\rangle_V \tag{6}$$

Here $\Gamma_m$ is given in $h^{-1}$, p in bar, and the relative gradient in $cm^{-1}$ units.

From Eqs. (1)–(3), (6), follows that for a well prepared glass cell filled with spin-polarized $^3$He gas at 2–3 bar pressure and the relative gradient below $10^{-3}$ $cm^{-1}$, the expected overall relaxation time is above 100 h.

## 3. Extraction of magnetic spin-relaxation rate in simulation and field mapping

According to (5) to estimate the magnetic relaxation rate, we need to estimate the relative magnetic field gradient of the transverse components of the field and average it over the cell volume. The standard procedure requires a preliminary adjustment of the 3-component magnetic probe with respect to the field direction, (the $Z$-axis must be oriented along the main component of the field). The gradient of the transverse components $\nabla B_1(\mathbf{x})$, and $\nabla B_2(\mathbf{x})$ is then measured as follows:

$$\boldsymbol{x} = \sum_{i=1,2,3} x^i \boldsymbol{e}_i \qquad \boldsymbol{\delta} = \sum_{i=1,2,3} \delta^i \boldsymbol{e}_i \tag{7}$$

$$\nabla B_j(x) = \sum_{i=1,2,3} \frac{1}{\delta^i}\left(B_j\left(\boldsymbol{x} + \frac{1}{2}\delta^i \boldsymbol{e}_i\right) - B_j\left(\boldsymbol{x} - \frac{1}{2}\delta^i \boldsymbol{e}_i\right)\right), \qquad j = 1,2 \tag{8}$$

where $\mathbf{e}_i$ denotes an orthonormal basis in the 3-dimensional space with the $\mathbf{e}_3$ basis vector oriented along the magnetic field. $\mathbf{x} = \{x^1, x^2, x^3\}$ is the point of interest and $\delta_i$ is the probe displacement parallel to the basis vector $\mathbf{e}_i$, i = 1, 2, 3. This simple procedure may be easily programmed in magnetic simulations, and performed in field mapping with a 3-D positioning robot and a 3-component magnetic probe. However, any change in the relative orientation of the field $\mathbf{B}(\mathbf{x})$ and the probe would require a realignment of the magnetic probe with respect to the field direction.

Since the goal of Pastis-3 is to perform neutron spin analysis for different orientations of the magnetic guide field at the sample position, the procedure described above is not convenient. To avoid the realignment of the probe for each orientation of the field $\mathbf{B}(\mathbf{x})$, we propose a new method to extract the magnetic relaxation rate of a confined polarized gas which works for an arbitrary orientation of the magnetic field and the probe, see Appendix.

As detailed in Appendix, the magnetic relaxation rate averaged over the volume V is given by:

$$\Gamma_m = D\frac{1}{\delta^2}\left\langle \sum_i \theta_i^2 \right\rangle_V, \qquad i = 1,2,3 \tag{9}$$

Here, $\theta_i$ is the angle between vector $\mathbf{B}(\mathbf{x} - (\delta/2)\mathbf{e_i})$ and $\mathbf{B}(\mathbf{x} + (\delta/2)\mathbf{e_i})$. The angle $\theta_i$ may be calculated from:

$$\theta_i = acos\frac{\boldsymbol{B}\left(\boldsymbol{x} - \frac{\delta}{2}\boldsymbol{e}_i\right) \cdot \boldsymbol{B}\left(\boldsymbol{x} + \frac{\delta}{2}\boldsymbol{e}_i\right)}{\left\|\boldsymbol{B}\left(\boldsymbol{x} - \frac{\delta}{2}\boldsymbol{e}_i\right)\right\| \left\|\boldsymbol{B}\left(\boldsymbol{x} + \frac{\delta}{2}\boldsymbol{e}_i\right)\right\|}, \qquad i = 1,2,3 \tag{10}$$

The average $\Gamma_m$ in the region of interest is estimated with Eq. (9). With the known $\Gamma_m$ and the known diffusion coefficient, the relative field gradients involved in (6) may be estimated by:

$$\langle G_{rel} \rangle_V \approx \left(\Gamma_m / D\right)^{1/2} \approx \left( \frac{1}{\delta^2} \left\langle \sum_i {\theta_i}^2 \right\rangle_V \right)^{1/2}, \qquad i = 1,2,3 \qquad (11)$$

## 4. PASTIS-3 overall concept

With the latest generation PASTIS-3 device, we aim to create a highly uniform magnetic field over a large volume and independent of the field direction, such that the overall relaxation time constant, $T_1$, of both NSF cells is above 100 h. Taking into account contributions from other sources of relaxation, this requirement means that the magnetic relaxation time, $T_m$, should be above 300 h. The magnetic device should have a wide (130 degree) shadow-free opening angle in the horizontal plane and ±6 degree in the vertical direction. To overcome the difficult field tuning with multiple correction coils that was unavoidable in PASTIS-2, we decided to use an iron-free magnetic system based only on current coils. To avoid problems with the adiabatic polarization transport and the spin-flipping in the incident beam part of the spectrometer, we have integrated into the PASTIS-3 device the incident beam polarizer, a $^3$He NSF with an AFP spin-flipper of polarized $^3$He gas [9,27,28].

**Magnetic design.** To create a highly homogeneous magnetic field with an arbitrary direction in space, we proposed a tilted coils design inspired by an idea of double-helix solenoids well known in superconducting magnets and in NMR technique [29–31]. The magnetic field is generated by two main pairs of coils, (B1 and B2), see Fig. 1b, inclined by the same angle $\Theta$. Powered by two independent DC power supplies, this configuration of coils can produce a magnetic field in the central region with any field direction in the ZY plane. The third orthogonal direction of the field, Bx, is created by mechanical rotation of the complete magnetic device around the vertical axis, the polarizer and the analyzer cells (rotation angle $\alpha$). For example, a vertical field direction in the central region is achieved when the DC current circulates in the same direction in both pairs of coils. A horizontal field direction demands the DC current in opposite directions in the two coil pairs. Changing the ratio of currents circulating in each pair allows to create a field $B_0$ inclined by any angle $\varphi$ in the ZY plane. The homogeneity of the central field region is largely improved with the addition of two compensation coil pairs (B1c and B2c), connected in series with their respective main coils to preserve the proportionality between their magnetic fields when the current is changing.

**Optimization.** The big advantage of the proposed "iron-free" coil system is the possibility to calculate the magnetic field in any point of space using known analytical solutions. This makes a numerical modeling and optimization of the magnetic coils highly effective and fast. To simulate the magnetic field created by each DC coil and to calculate, the effective relaxation rate, we used the package Radia [32] working under "Wolfram Mathematica" [33]. For the optimization of the coil sizes and their positioning, we used a package of global optimization in Mathematica based on the "Differential Evolution" algorithm [34].

The magnetic field in the central region is built as a superposition of fields created by 8 DC coils. The twofold rotation symmetry of the coil assembly around the $X$-axis reduces the number of independent coils to 4. The field in an arbitrary point due to a circular coil of finite size depends on the outer radius of the coil $R_{out}$, the height and width of the coil section, h and w, the position of the coil center p along the coils symmetry axis, the current density I and the inclination of the symmetry axis $\Theta$. Based on this 4-coil pair system, we build a numerical field map in the toroidal region of interest $\Omega$ where the polarizer and the analyzer cells are installed and calculate the volume averaged relaxation rate given by Eq. (9). $\Omega$ is a toroidal volume with rectangular cross section of inner radius 60 mm, outer radius 130 mm and 50 mm height, which includes the cells at any rotation angle $\alpha$ of the coil system around the vertical axis. The relaxation rate within $\Omega$ was used as a Figure-of-Merit for the global optimization procedure. The optimization was performed with the field along Y as this gives the highest value of the relaxation rate and current density.

**Table 1**
Dimensions of the PASTIS-3 coils. Outer radius $R_{out}$, position of the coil center along the symmetry axis p, number of turns/layer $N_{turns}$, number of layers $N_{layers}$, section of the coil in height h and width w. I is the current density required to create 2 mT field in the Y direction. $\Theta$ is the angle between each coil pair axis and the Z-axis, within the ZY plane.

| Coil | $R_{out}$ (mm) | p (mm) | $N_{turns}$ | $N_{layers}$ | h (mm) | w (mm) | I (A/mm$^2$) | $\Theta$ (rad) |
|---|---|---|---|---|---|---|---|---|
| B1 | 316.00 | **159.94** | 12 | 9 | 36.60 | 15.53 | 5 | $\pi$/16 |
| B2 | 288.00 | **144.07** | 11 | 9 | 33.55 | 15.53 | −5.2 | |
| B1c | **256.97** | **134.20** | 6 | 6 | 18.30 | 10.35 | −5 | |
| B2c | **238.37** | **122.37** | 6 | 6 | 18.30 | 10.35 | 5.2 | |

To minimize the number of free parameters in the optimization, and to comply with the design and technical constraints, we set some of the parameters using the following process: The increase of the radius of the main coils B1 and B2 results in a lower relaxation rate, the outer radius of B1 and B2, $R_{out,B1}$ and $R_{out,B2}$ is therefore fixed to the maximum possible within the space limitations. The compensation current is chosen opposite to the current in the respective main coil to allow a larger distance between upper and lower coil parts, and thus gain in the vertical opening angle for the neutron beam. We fixed the maximum current densities $I_{B1}$ and $I_{B2}$, to limit the thermal expansion of the water-cooled coils, and the angle $\Theta$ was adjusted as $\pi$/16 to provide the desired vertical opening angle and to produce sufficient field in the Y-direction. The calculated maximum thermal expansion of the coils was then limited to 0.1 mm, for $R_{out,B1}$ which fulfill the precise coils geometry required. All individual coil sections (h and w) were defined as discrete number of layers ($N_{layers}$) with discrete number of turns in the layer ($N_{turns}$). We decided to build all the coils from the same rectangular wire size (3.05 × 1.73 mm$^2$ including insulation) for technical reasons in the precise coils production and to power them with standard current supplies. We optimized all coil sections in an iterative process to avoid mechanical crossing of left/right coils within the space limitations (outer diameter 690 mm and inner diameter 390 mm), and to provide sufficient field in the center. In the last stage of the optimization process, we used 6 free parameters, the position of the four coil centers along the symmetry axis ($p_{B1}$, $p_{B2}$, $p_{B1c}$, $p_{B2c}$), and the two outer radii of the compensation coils ($R_{out,B1c}$, $R_{out,B2c}$).

The coils parameters found using this procedure are given in Table 1.

Fig. 2 shows the simulated magnetic field gradients for both polarizer and analyzer cells leading to the very long relaxation times $T_m$ @ 1bar >> 2000 h for any angle $\varphi$ and $\alpha$. During the coils optimization, we also study the stability of the optimal configuration with respect to possible deviations from the optimal parameters (coil sizes, positions, tilt, non-concentricity). As an example, Fig. 3 shows the stability of $T_m$ with respect to deviations from the ideal Z position of one main coil B2, when the field is in the Y direction. This study allowed us to conclude that with realistic tolerances in the coil production and the assembling, we may expect the global relaxation times $T_m$ to be higher than 500 h for a 2bar NSF cell and any field direction.

Apart from the magnetic gradients that are inherent to the magnetic coils, there are always gradients due to the magnetic environment of the spectrometer, and these extra-gradients may be not negligible. We performed a magnetic field mapping on IN20, where PASTIS-3 is planned to be used and found typical gradients of the order $10^{-3}$ mT/cm, an order of magnitude higher than the gradients from PASTIS-3 alone. For a 1 mT holding field commonly used at the ILL for $^3$He NSF cells, this external gradient results in $T_m \approx 140$ h for a 1bar $^3$He cell. To reduce the influence of the external field gradient further, we raised the PASTIS-3 holding field to 2 mT which should result in 4 times longer $T_m$.

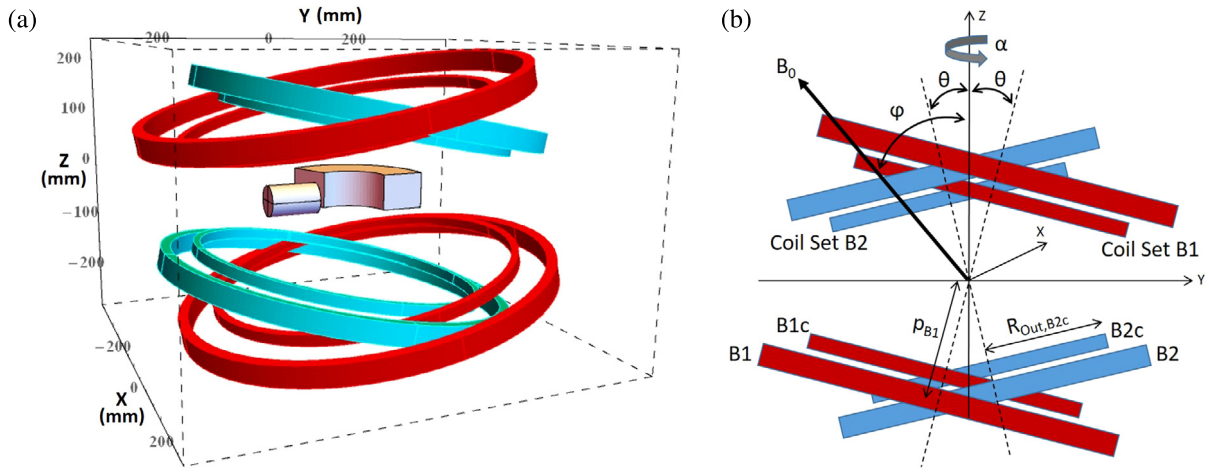


**Fig. 1.** (a) Concept of the magnetic design of PASTIS-3. The banana-shaped analyzer as well as the polarizer cell are schematically shown. (b) Two sets of compensated coil pairs B1 (red) and B2 (blue) tilted from the $Z$-axis by the same angle $\Theta$ provide a field $B_0$ in the plane of the two inclined coil-symmetry axes, so that $B_0$ is at an angle $\varphi$ from Z. $\alpha$ is the rotation angle of the entire coil set around the vertical axis. When the field $B_0$ is in the YZ-plane, $\alpha = 0$. The coil set including the mechanics fits into a diameter of 70 cm, the standard size for sample environment on IN20.. (For interpretation of the references to color in this figure legend, the reader is referred to the web version of this article.)

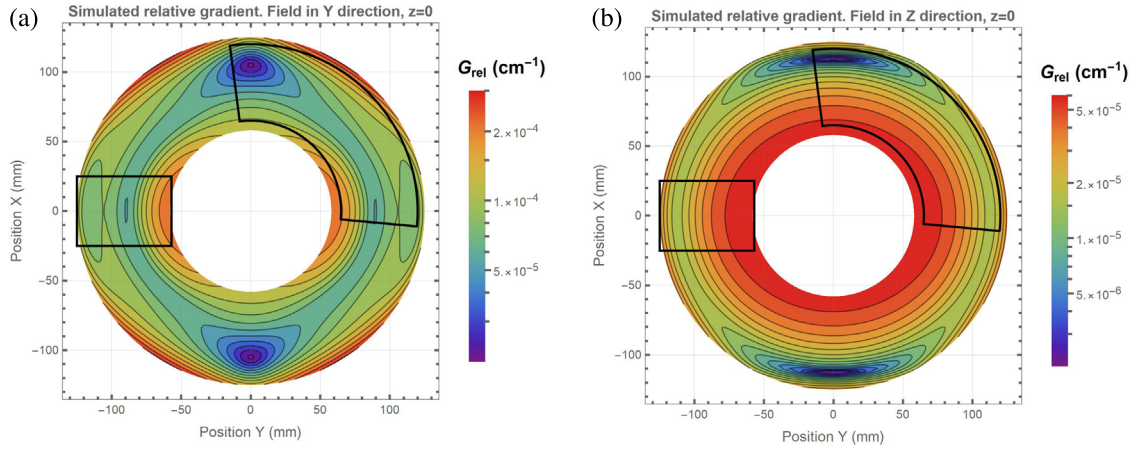


**Fig. 2.** Simulation, of the relative gradient in the equatorial plane with the field in the Y (a) and Z (b) direction, respectively (notice the different scales). The volume averaged gradient in the region $\Omega$, a toroidal volume with rectangular cross section of inner radius 60 mm, outer radius 130 mm and 50 mm height that contains the region of both cells for any angle $\alpha$, is $\langle G_{rel}\rangle_V = 1.6 \times 10^{-4}$ cm$^{-1}$ for $B_Y$ (a) and $\langle G_{rel}\rangle_V = 5\times10^{-5}$ cm$^{-1}$ for $B_Z$ (b), which correspond for a 1 bar cell to $T_m$ = 5610 h for $B_Y$ and $T_m$ = 59 210 h for $B_Z$. The two cells are represented in their respective position when the angle $\alpha$ around the vertical axis is equal to zero. (Color online).

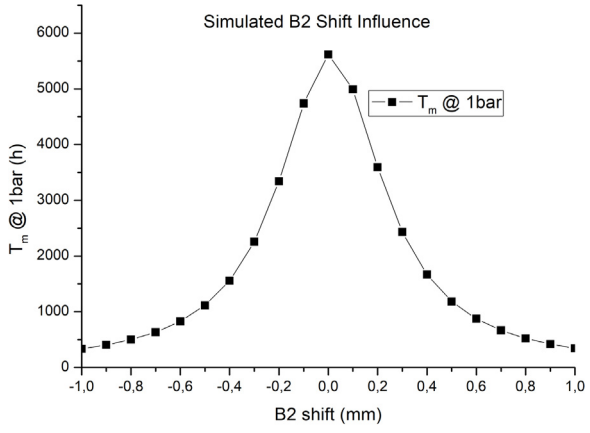


**Fig. 3.** Simulated influence of the shift of one main coil (B2) away from the ideal Z position on the magnetic relaxation time, for a $^3$He pressure of 1 bar, in the region $\Omega$. The field is parallel to Y, ($\varphi$ = 90 degrees).

**Discussion on the angle Θ.** The angle $\Theta$ is an important parameter of the device as it act on the maximum vertical opening angle possible and on the value of the field. When $\Theta$ is close to 0, than it is difficult to produce large field in the Y direction for an acceptable current density in the coils (see Eq. (12)). At the other limit, when $\Theta$ is close to $\pi/2$, the difficulty is transferred to the production of the field in the Z direction. In this respect, the optimum would be when $\Theta$ is $\pi/4$, but for this geometry, there would be blind angles in the scattering planes created by the finite thickness of the coils. The angle $\Theta$ also play an important role in the iterative optimization process as it changes the outside diameter of the device, the space available where the coils are crossing and so the coils possible cross-sections. The choice of the practical $\Theta$ depends on the instrument (opening angle, magnetic environment, space limitations).

As an example, to increase the opening angle, one may reduce $\Theta$ from the PASTIS-3 value of $\pi/16$ to $\pi/32$, keeping all other parameters the same as in Table 1, then the magnetic relaxation time, for a $^3$He pressure of 1 bar, in the $\Omega$ region will decrease from $T_m$ = 5610 h to $T_m$ = 2220 h. Optimization using the 6 free-parameters described above results in $T_m$ = 3500 h, however, due to the upper limit imposed on the maximum coil currents, this result corresponds to half the magnetic field amplitude (1 mT instead of 2 mT) and increase the sensitivity to external field gradients.

**Fig. 4.** "Cassette" for water cooling and high-precision positioning of the four coils. Only the lower part of the cassette is shown, the upper part, which makes it watertight, is missing.

## 5. PASTIS-3 components

### Coils

The space available on IN20 for the PASTIS-3 device is a cylindrical cavity of 700 mm diameter. The request of a large volume of the desired field homogeneity region together with the request of a 2 mT holding field amplitude imply a current density of up to 5 A/mm $^2$ in the coils, which demands water cooling to limit the thermal expansion of the coils, in particular when the field is along the Y direction at 2 mT. To conciliate the space limitations, the high current density, and the water cooling, we decided to build frame-free coils immersed in two water tanks above and below the horizontal scattering plane (Fig. 4). A 5 kW deionized water chiller controls the circulating cooled water as the maximum total power dissipation of all coils is 3 kW. The average increase in the coils temperature was preliminary estimated and later checked via coil resistances measurement to be below 10 °C. The coils were built in-house from rectangular enameled 3.05 × 1.73 mm$^2$ copper wire, then immersed in a special epoxy resin and baked to freeze the wire position. Although we paid attention to precision manufacturing of the DC coils, the final sizes were found within ± 0.3 mm from the optimal. These deviations in the coil dimensions were taken into account in the second stage of the magnetic device optimization where for a fixed size of coils, only the coil positions were re-tuned.

### $^3$He polarizer and analyzer cells and valves

The polarizer and the analyzer cells are made with monocrystalline silicon windows on the neutron path to reduce neutron scattering from the windows, and to define the path length of the neutron in the $^3$He precisely (Fig. 5). The polarizer is a cylindrical 5 cm diameter cell, 7 cm long, with molecular bonded 3 mm thick silicon windows realized at the ILL. The analyzer [10] is a banana shaped cell ( $R_{inner}$ = 6.5 cm, $R_{outer}$ = 12 cm, height 5 cm) with curved 5 mm thick silicon windows on 102 degrees in the horizontal plane (inner dimensions given for both cells). The analyzer cell covers largely the 75 degree range of scattering angles covered by the multi-analyzer FlatCone, and we can rotate the cell to cover the full 130 degree range allowed by PASTIS-3.

Each of polarizer/analyzer cells are equipped with "in-house" developed remote-controlled non-magnetic valves. The body of the valves is made of aluminum and titanium alloy — the same materials as used for the compressor of the Tyrex filling station. The valve is spring-loaded to remain closed when not in use and is opened by applying compressed air. The gas relaxation due to the pneumatic valve is optimized by minimizing the area of the metallic surface seen by the polarized gas in the spin-filter cell. When the remote-controlled valve is closed, only 7 mm$^2$ of metallic surface is accessible to the gas. The capillary between the cell and the pneumatic valve is made of Pyrex. The influence of the pneumatic valve on the wall-relaxation time of the cell is negligible, the corresponding relaxation time was found > 1000 h. The pneumatic valve is also mechanically stable. It has been opened and closed hundreds of time without any perceptible hysteresis in its performance.

**Table 2**
Wall relaxation times of the PASTIS-3 cells after correction for dipole relaxation and gradient relaxation time ($T_m$ ≈ 14 000 h @ 1 bar for the "test bench"). The loss due to the NMR FID technique is negligible and not taken into account. It depends on the time between the pulses, which was chosen as a function of the approximate $T_1$, such as to make these losses negligible. The tests on IN20 described further below refer to the Si/C5.4/3He/04 polarizer cell and the Si/Pastis3/03 analyzer cell.

| Polarizer | $T_w$ (h) ± 10 h | Analyzer | $T_w$ (h) ± 2 h |
|---|---|---|---|
| Si/C5.4 × 7/3He/03 | 163 | Si/Pastis3/01 | 38 |
| **Si/C5.4 × 7/3He/04** | **340** | Si/Pastis3/02 | 30 |
| Si/C5.4 × 7/3He/05 | 240 | **Si/Pastis3/03** | **109** |
| Si/C5.4 × 7/3He/09 | 70 | Si/Pastis3/04 | 37 |
| Si/C5.4 × 7/3He/10 | 28 | Si/Pastis3/05 | 85 |

Five polarizer and analyzer cells were built from silicon and Borofloat parts glued or molecular bonded together, then all cells were coated with rubidium. The spin-relaxation time in each cell was measured in "Laboratory conditions". For this we filled each cell with polarized $^3$He on the "TYREX" MEOP station at the ILL [4] at 0.5 bar, placed them in a highly homogeneous magnetic field ($\langle G_{rel} \rangle_V \approx 10^{-4}$ cm$^{-1}$) of the "Test Bench" (Magnetic device for $T_1$ measurement in our laboratory) and measured the spin-relaxation time constant with the free induction decay (FID) technique [7]. The measured wall relaxation time constants are listed in Table 2. The lower values for the analyzer cells are still under investigation and probably are related to magnetic impurities in the Borofloat parts and glue. For PASTIS-2 [10] we succeeded to build "banana" shaped cell with ≈ 300 h wall relaxation time. Unfortunately, this cell was disassembled following a leak and cannot be further used as a NSF. Nevertheless, the positive experience in the production of such an excellent analyzer cell proves that it is possible to achieve very high relaxation times with this type of cell.

### Adiabatic fast passage $^3$He flipper

In PASTIS-3 the polarization of the incident neutron beam can be "flipped" by inverting the polarization of the $^3$He gas in the polarizer NSF cell. This inversion is achieved by the Adiabatic Fast Passage technique. An amplitude modulated radio-frequency sweep signal with a span of 16 kHz and a central frequency equal to the Larmor frequency (≈ 32 kHz) in the holding magnetic field (1 mT) is applied to the gas for a time interval $\Delta t \approx 3$ ms long in comparison with a Larmor period and short in comparison with the spin relaxation time constant in the applied RF field. The Gaussian shaped envelope has a maximum amplitude of ≈ 0.1 mT.

To reduce the impact of the polarizer RF field leakage on the NSF analyzer cell during the spin-flip signal, we confined the polarizer RF coil into a closed aluminum box [27], see Fig. 6. In order to minimize RF field leaks through material gaps, most of the box is directly machined from an aluminum block. Both the input and output windows have a reduced thickness (1 mm versus 3 mm of the main body) to maximize the neutron transmission. The residual amplitude of the RF field at the position of the analyzer cell is estimated to be below $10^{-4}$ mT for 3 mm aluminum (skin depth @ 32 kHz ≈ 0.46 mm). The polarization losses were measured off-line by monitoring the initial and final $^3$He polarization with the FID NMR technique. We applied 50 000 flips within 3 h, and determined the $^3$He polarization loss per single flip as $7 \times 10^{-6}$ for the polarizer cell and $2 \times 10^{-5}$ for the analyzer cell, both filled with 1 bar $^3$He. Therefore, during a 24 h experiment with a few hundreds of flips, the influence of the flipper on the relaxation rate of the $^3$He polarization in the cells is negligible.

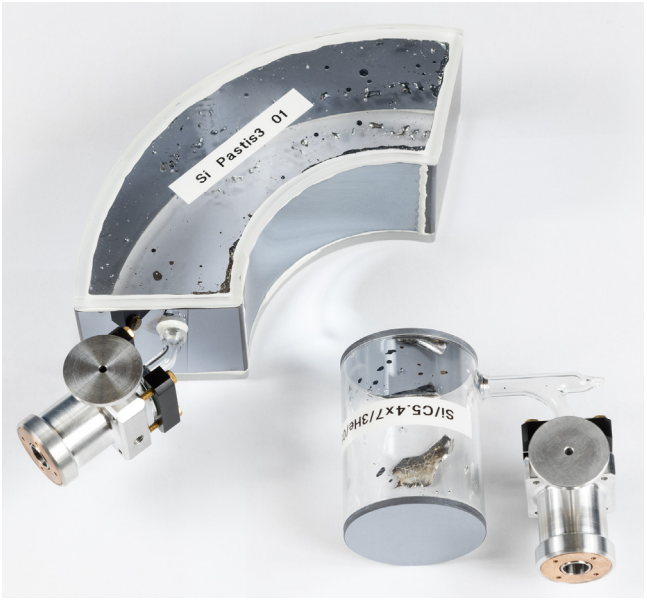


**Fig. 5.** Coated polarizer (cylindrical cell: 5 cm diameter and 7 cm long with 3 mm thick silicon windows) and analyzer cells (banana shaped cell: $R_{inner}$ = 6.5 cm, $R_{outer}$ = 12 cm, height 5 cm with curved 5 mm thick silicon windows on 102 degrees in the horizontal plane) equipped with pneumatic valves.

## 6. PASTIS-3 characterization

### Field rotation method

Assuming that two sets of compensated coils pairs are tilted by the same angle $\Theta$, the field components $\{B_y, B_z\}$ in the central region may be written as follows:

$$\begin{cases} B_y = B_0 sin\varphi = (A_1 I_1 - A_2 I_2) sin\theta \\ B_z = B_0 cos\varphi = (A_1 I_1 + A_2 I_2) cos\theta \end{cases} \quad (12)$$

Here $B_0$ and $\varphi$ are the desired field amplitude and the angle from the Z direction in the YZ plane, $I_1$ and $I_2$ are DC currents circulating in each set of compensated coil pairs, and $A_1$,$A_2$ are coefficients (in Gauss/Amps) relating the coil currents with the generated field. Solving Eq. (12) for $I_1$ and $I_2$ yields:

$$I_1 = \frac{B_0}{2A_1}\left(\frac{\cos\varphi}{\cos\theta} + \frac{\sin\varphi}{\sin\theta}\right) and\, I_2 = \frac{B_0}{2A_2}\left(\frac{\cos\varphi}{\cos\theta} - \frac{\sin\varphi}{\sin\theta}\right) \quad (13)$$


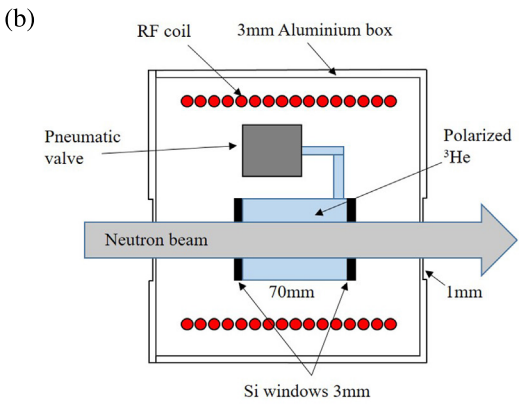


**Fig. 6.** Picture (a) and scheme (b) of the polarizer AFP flipper box (13 × 10 × 15 cm) and cover. The box includes the RF coil and the 5 cm diameter polarizer cell equipped with pneumatic valve.

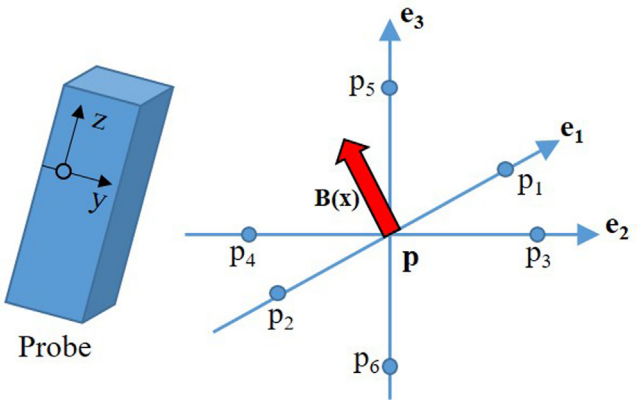


**Fig. 7.** Scheme of field mapping. Point of interest p = {$x_1$, $x_2$, $x_3$} and 6 points $p_1$, $p_2$,... $p_6$ displaced by ± $\delta/2$ in 3 orthogonal directions $\mathbf{e}_i$, i = 1, 2, 3. The 3-component magnetic probe has an arbitrary orientation with respect to the magnetic field **B(x)** and the 3-D robot coordinate system {$\mathbf{e_1}$, $\mathbf{e_2}$, $\mathbf{e_3}$}.

As already mentioned, the angle $\alpha$ around the vertical axis is controlled by mechanical rotation of the coils.

### Field mapping results

To qualify the PASTIS-3 magnetic fields, we mapped the field gradients in the central region of Pastis-3 using a three-dimensional mapping robot equipped with a 3-component, XYZ, fluxgate (Wuntronic WFG-130) with 3 mT range. To diminish the long-term drift of the probe, all 3 components of the magnetic field **B(x)** were measured successively in 6 points displaced from the target point p by ± $\delta/2$ in 3 orthogonal directions {$\mathbf{e_1}$, $\mathbf{e_2}$, $\mathbf{e_3}$}, $\delta$ = 10 mm, see Fig. 7, taking into account the different positions of the sensors in the probe. From these data's, we extract all angles $\theta_i$ according to (10) and calculate $\Gamma_m$ and $\langle G_{rel}\rangle_V$ according to (9) and (11). The averaging was performed over 180 target points within the region of interest $\Omega$. The magnetic field amplitude was set to 1.8 mT. From repetitive measurements of the known magnetic field of TYREX and our "Test bench", we estimate the accuracy of our field mapping technique to be close to $10^{-4}$ $cm^{-1}$ in terms of the relative gradient $\langle G_{rel}\rangle_V$ within those conditions.

All together 8 directions of the magnetic field in the YZ plane were mapped, with tilt angle from the $Z$-axis $\varphi$ = 0, 45, 90, 135, 180, 225, 270 and 315 degrees. Results for the $^3$He cell at 1 bar are shown in Table 3.

Comparing results of field mapping, (Fig. 8), with the simulation results (Fig. 2), (as well as data shown in Table 3), we conclude that the measured residual field gradients are a factor 2–5 times higher that one could expect from the simulation. This difference may be explained

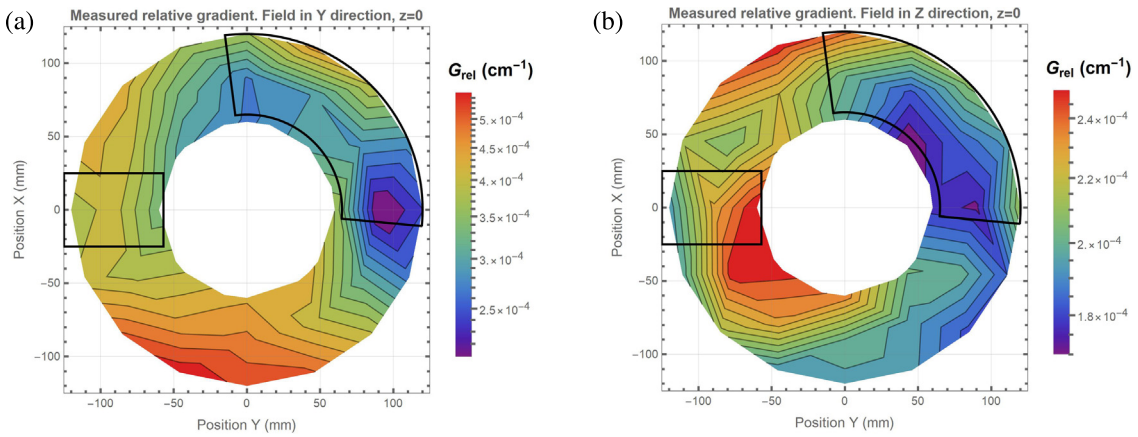


**Fig. 8.** Measured relative gradients $G_{rel}$ in the equatorial plane with the field in the Y (a) and Z (b) direction respectively (notice the different scales). The volume averaged gradient in the region $\Omega$, that contains the region of both cells for any angle $\alpha$ is $\langle G_{rel}\rangle_V = 4.1 \times 10^{-4}$ cm$^{-1}$ for $B_Y$ (a) and $\langle G_{rel}\rangle_V = 2.2 \times 10^{-4}$ cm$^{-1}$ for $B_Z$ (b), which correspond for a 1 bar cell to $T_m$ = 850 h for $B_Y$ and $T_m$ = 2950 h for $B_Z$. The two cells are represented in their respective position when the angle $\alpha$ around the vertical axis is equal to zero. (Color online).

**Table 3**
Measured magnetic relative gradients averaged over 180 local points within $\Omega$, measured for different field angles in the YZ plane and respective calculated relaxation times $T_m$ for 1 bar $^3$He pressure. The simulated $T_m$ are shown in the last column.

| Angle $\varphi$ from Z direction (degree) | From field mapping Eq. (11) $\langle G_{rel}\rangle_V$ ($10^{-4}$ cm$^{-1}$) | From field mapping Eq. (9) $T_m$ @ 1 bar (h) | Simulated $T_m$ @ 1 bar (h) |
|---|---|---|---|
| 0 | 2.2 | 2950 | 59 210 |
| 45 | 2.7 | 1960 | 8670 |
| 90 | 4.1 | 850 | 5610 |
| 135 | 3.2 | 1395 | 16 270 |
| 180 | 1.5 | 6350 | 59 210 |
| 225 | 3.2 | 1395 | 8670 |
| 270 | 5.0 | 570 | 5610 |
| 315 | 4.0 | 895 | 16 270 |

by residual stray fields from the external magnetic environment, deviations of the real coil geometry from the ideal geometry, and the real positioning of the coils. Also the limited stability of the magnetic probe, the magnetic environment and the DC power supplies limits the precision of field mapping procedure at the level of $10^{-4}$ cm$^{-1}$. Everything below this limit is not within our scope. Indeed, even for relative magnetic gradients shown on Fig. 8, the expected relaxation time for a 2 bar $^3$He NSF polarizer and analyzer cells is of the order and above 1000 h.

## PASTIS-3 installed on IN20

To test PASTIS-3 under realistic experiment conditions, it was installed on the thermal triple-axis spectrometer IN20 at the ILL, equipped with Si(111) monochromator, Orange cryostat, and FlatCone multi-analyzer. For all the tests in this section, we measured the $^3$He polarization with the free induction decay (FID) nuclear magnetic resonance (NMR) method and we inverted the $^3$He polarization in the polarizer cell with the adiabatic fast passage (AFP) technique.

### *Polarization losses during cell insertion*

We expect that the homogeneity of the PASTIS-3 magnetic field will allow us to recharge the polarizer/analyzer NSF cells only once in 24 h. The delicate point of the cell-change procedure is the introduction of the cells from the transporter field [35] into the field of PASTIS-3 in the magnetic environment of the spectrometer. Remember that the field outside the DC coil is opposite to the field in the central region and, therefore, there is a risk to depolarize the "fresh" cell at the insertion while crossing a zero-field region. To avoid this possibility, we introduce the NSF cells into the central region of PASTIS-3 in the "Earth-magnetic field", followed by a 5 s linear increase of the field to a nominal value of 1.8 mT in the earth field direction. This test was realized with both cells filled at 1 bar, by measuring the initial/final FID signal amplitude and repeating the operation several times to increase the precision. We found the insertion losses to be of the order of 0.6%.

### *Flipper tests*

We verified the impact of the $^3$He AFP flipper on the polarizer and analyzer polarization by applying 10 000 flips. The $^3$He polarization loss for the polarizer at 1 bar (2.5 bar) was found $5 \times 10^{-5}$ ($2.2 \times 10^{-5}$) per flip and the associated loss, from RF leakage, in the analyzer cell at 1 bar (1.45 bar) was $4 \times 10^{-5}$ ($3.2 \times 10^{-5}$) per flip. This should be compared with the loss of $7 \times 10^{-6}$per flip for the polarizer and $2 \times 10^{-5}$ per flip for the analyzer measured at 1 bar in the laboratory as described earlier. The differences may arise from RF reflections in the tubular frame of PASTIS-3 or on the cryostat tail. From these measurements, we conclude that the flipper-induced polarization losses are marginal since they represent an extra relaxation time above 1000 h when flipping every 2 min. (During an inelastic measurement, we flip approximately every 5 min, not more than 300 times per 24 h.)

### *Field rotation*

To verify the possible influence of DC current manipulations required to control the direction of the PASTIS-3 field on the spin-relaxation of the polarizer/analyzer cells, we performed continuous field rotations over 240 full turns (360°) of the magnetic field direction in the YZ plane. The speed of rotation was limited by the instrument control software and was much lower than the Larmor frequency $\omega_{rot} = 1/15$ s$^{-1} \ll \omega_{Larmor}$. As expected, we observed no measurable extra-relaxation of the $^3$He polarization due to the field rotation.

### *Relaxation times*

We verified the overall relaxation time in situ on IN20 with an analyzer cell (Si/Pastis3/03) filled with $^3$He at 2.3 bar and a polarizer cell (Si/C5.4x7/3He/04) filled at 2.7 bar (see Table 2). On the laboratory "Test bench" with known low gradient field, these cells have wall relaxation times of 340 h and 109 h, respectively. On IN20, a 1.8 mT field was rotated by 90 degrees every 30 s in complete 360 degree circles. The $^3$He polarization in the polarizer cell was inverted by the AFP flipper every time the field was in Z direction by decreasing field to 1 mT, applying the RF signal and restoring the field to 1.8 mT (the full flipping procedure time ≈ 2 s). We repeated this sequence during 19 h for a total of 470 flips and full 360 degree rotations of the field. The initial and final $^3$He polarization were measured with FID to calculate the overall relaxation time in both cells ($T_{1,FID}$ in Table 4).

Table 4 shows $T_{1,FID}$ together with $T_d$, the dipole–dipole relaxation constant (see, Eq. (1)), $T_{flip}$, the calculated additional relaxation induced by the flipper, $T_{1,0}$ which represents the relaxation for an ideal (zero gradient) magnetic field, $T_{m,map}$, the expected magnetic relaxation

**Table 4**
Expected and measured ($T_{1,FID}$) relaxation times in polarizer/analyzer cells in-situ on IN20.

| Cell | Pressure bar | $T_w$ h | $T_d$ h | $T_{flip}$ h | $T_{1,0}$ h | $T_{m,map}$ h | $T_{expected}$ h | $T_{1,FID}$ h | $\langle G_{rel}\rangle_V$ $10^{-4}$ cm$^{-1}$ |
|---|---|---|---|---|---|---|---|---|---|
| Polarizer | 2.7 | 340 | 302 | 2160 | 149 | 3240 | 142 | **112** | 9.3 |
| Analyzer | 2.3 | 109 | 355 | 2300 | 80 | 2760 | 78 | **64** | 10.3 |

time based on the results of the field mapping averaged in the field directions used during the experiment, and scaled to the actual cell pressure, and $T_{expected}$, the expected cumulative effect of $T_w$, $T_d$, $T_{flip}$ and $T_{m,map}$. We found that the measured relaxation times in-situ on IN20 are lower than the values expected from field mapping in the lab, both for the polarizer and the analyzer cell. This fact implies that on IN20, the external field gradients are higher than the internal gradients of PASTIS-3. The last column in Table 4 displays the calculated relative gradient $\langle G_{rel}\rangle_V$, which would explain the measured in-situ values of $T_{1,FID}$. Those field gradients are at least 3 times higher than expected from the field mapping in the laboratory ($\langle G_{rel}\rangle_V \approx 3.10^{-4}$ cm$^{-1}$).

***External gradients from the spectrometer environment***

Prior to the installation of the magnetic device on IN20 for neutron tests, we tried to identify the main sources of external field gradients over the cell volumes. Despite the application of a routine demagnetization procedure as described in ref [27], after each use of a high-field superconducting magnet on IN20, some magnetic gradient sources still remain close to the PASTIS-3 device. We identified two major sources: the bearings in the sample table onto which PASTIS-3 is installed (4 units with 600 mm diameter) and the stray fields of the permanent magnets in the monochromator radiation protection. We demagnetized the bearings using a Bulk Degausser (Verity systems SV91m). The guide field in the monochromator protection generates a stray field mainly in the Z direction with an amplitude that decays along the neutron path and produces field variations of the order of $10^{-3}$ mT/cm. The induced relative gradient over the cell volume in the 2 mT field of PASTIS-3 is about $5 \times 10^{-4}$ cm$^{-1}$. The stray field was reduced it to ≈ 20%–30% of its strength by a supplementary guide field with opposite field direction at the exit of the monochromator protection.

## 7. Neutron measurements

The first inelastic neutron scattering test with PASTIS-3 was performed on IN20 in February 2020 (Fig. 9) using the FlatCone multi-analyser detector unit with final neutron wavelength of 2.09 Å, and the Si(111) monochromator with incident wave lengths of 2.09 Å, 1.94 Å or 1.9 Å, providing the different desired energy transfers. Every day, the polarizer cell ($T_w$=340 h, 3 bar $^3$He pressure) and the analyzer cell ($T_w$ = 109 h, 2.3 bar) were refilled on the TYREX MEOP filling station and transported to the instrument. During this test, the field angles $\varphi$ and $\alpha$ varied according to the needs of the experiment. Details of the experiment, the data acquisition and treatment will be published in a forthcoming article.

To verify the relaxation time, the $^3$He polarization was systematically determined at the beginning and end of an experiment section by non-polarized neutron transmission measurements on a sample Bragg peak. The transmission of each cell was measured by moving the cell in and out of the beam using the motorized translation stages of PASTIS-3, with the respective other cell translated out of the beam. After correction for detector deadtime, the $^3$He polarization of the cells was extracted via the non-polarized neutron transmission Eq. (14). The homogeneity of the PASTIS-3 device in the cell positions outside the beam is sufficiently good to permit such transmission measurements of the individual cells without significant polarization loss ($T_m$ = 300 h at 2 bar pressure in vertical field and 80 mm outside the beam).

$$T = T_c exp(-O)\cosh(OP_{He}) \tag{14}$$

$$O = \lambda\ [\mathrm{A}] * L\ [\mathrm{cm}] * p\ [\mathrm{bar}] * 21.482/T\ [\mathrm{K}] \tag{15}$$

Here $T_c$ is the cell window transmission, $P_{He}$ is the $^3$He polarization and O is the opacity of the $^3$He gas proportional to the pressure p, neutron wavelength $\lambda$, and length of the cells L.

The initial $^3$He polarization in both cells after insertion in the PASTIS-3 device was found between 76% and 79%. The overall cell relaxation times, found from 12 sets of transmission measurements, differ a little from one day to another, and correspond to 116.4 h ± 6.3 h, and 72.3 h ± 1.8 h for the polarizer and analyzer respectively. During the experiment, the $^3$He polarization in the polarizer cell was inverted every 5 min. Results are given in Table 5.

**Table 5**
Expected and measured ($T_{1,neut}$) relaxation times in polarizer/analyzer cells in-situ on IN20 from the first neutron test (Feb 2020). $T_{1,neut}$ is the overall relaxation time constant resulting from neutron transmission measurements as described in the text.

| Cell | Pressure bar | $T_w$ h | $T_d$ h | $T_{flip}$ h | $T_{1,0}$ h | $T_{m,map}$ h | $T_{expected}$ h | $T_{1,neut}$ h | $\langle G_{rel}\rangle_V$ $10^{-4}$ cm$^{-1}$ |
|---|---|---|---|---|---|---|---|---|---|
| Polarizer | 3 | 340 | 272 | 5000 | 147 | 3600 | 141 | **116** | 8.7 |
| Analyzer | 2.3 | 109 | 355 | 4790 | 82 | 2760 | 80 | **72** | 7.3 |

Comparing the relaxation times "in-situ" with the expected $T_{expected}$ given in Table 5, we conclude that our "magnetic cleaning" procedure reduces the effective field gradient from $\langle G_{rel}\rangle_V \approx 9.3 \times 10^{-4}$ cm$^{-1}$ to $\langle G_{rel}\rangle_V \approx 8.7 \times 10^{-4}$ cm$^{-1}$ on the polarizer cell and from $\langle G_{rel}\rangle_V \approx 10.3 \times 10^{-4}$ cm$^{-1}$ to $\langle G_{rel}\rangle_V \approx 7.3 \times 10^{-4}$ cm$^{-1}$ on the analyzer cell.

A second test was realized in September 2020. The replacement of the closest bearing in the spectrometer table by a non-magnetic one, has led to an improvement of the external stray field. The field rotation and flipping frequency were identical to the test in February 2020. The results are shown in Table 6. The measured overall cells relaxation times correspond to 150 h ± 10 h and 78 h ± 3 h respectively. From these data, we extract even smaller value of the effective gradient $\langle G_{rel}\rangle_V \approx 5 \times 10^{-4}$ cm$^{-1}$, which approaches the field mapping value of PASTIS-3 in laboratory environment ($\langle G_{rel}\rangle_V \approx 3 \times 10^{-4}$ cm$^{-1}$).

Even a lower stray field from the magnetic environment would further improve the PASTIS-3 performance, we expect a considerably larger effect from improving the wall relaxation time of the analyzer cell, (compare $T_w$ = 109 h in the current experiment with $T_w$ = 300 h in [10]).

**Table 6**
Expected and measured relaxation times in polarizer/analyzer cells in-situ on IN20 from the second neutron test (Sept 2020).

| Cell | Pressure bar | $T_w$ h | $T_d$ h | $T_{flip}$ h | $T_{1,0}$ h | $T_{m,map}$ h | $T_{expected}$ h | $T_{1,neut}$ h | $\langle G_{rel}\rangle_V$ $10^{-4}$ cm$^{-1}$ |
|---|---|---|---|---|---|---|---|---|---|
| Polarizer | 2 | 340 | 408 | 3330 | 176 | 2400 | 164 | **150** | 5.3 |
| Analyzer | 2.1 | 109 | 389 | 4375 | 84 | 2520 | 81 | **78** | 5 |

## 8. Conclusion

We have designed, built and tested a new PASTIS-3 device for wide-angle XYZ polarization analysis, PASTIS-3, on the thermal triple axis spectrometer IN20 at the ILL. It contains an iron-free magnetic system, a $^3$He NSF polarizer, a $^3$He spin flipper and a $^3$He NSF wide-angle analyzer. The new magnetic design allows to polarize and to control polarization of the incident beam, to maintain blind-angle-free wide-angle (130 degrees) XYZ spin-analysis employing two independent polarized $^3$He NSF cells. Moreover, it allows to perform polarization analysis for any direction of the magnetic field at the sample. The $^3$He magnetic relaxation time due to the device's field inhomogeneity was found to be >1000 h @ 2 bar, averaged over all the field directions. The integrated AFP flipper of the polarizer NSF allows to flip the incident polarization as often as every 2 min, this would induce an additional polarization decay with a time constant of the order of 1000 h. Overall, the performance of PASTIS-3 is presently limited only by stray fields from the magnetic environment of the spectrometer, and by the wall

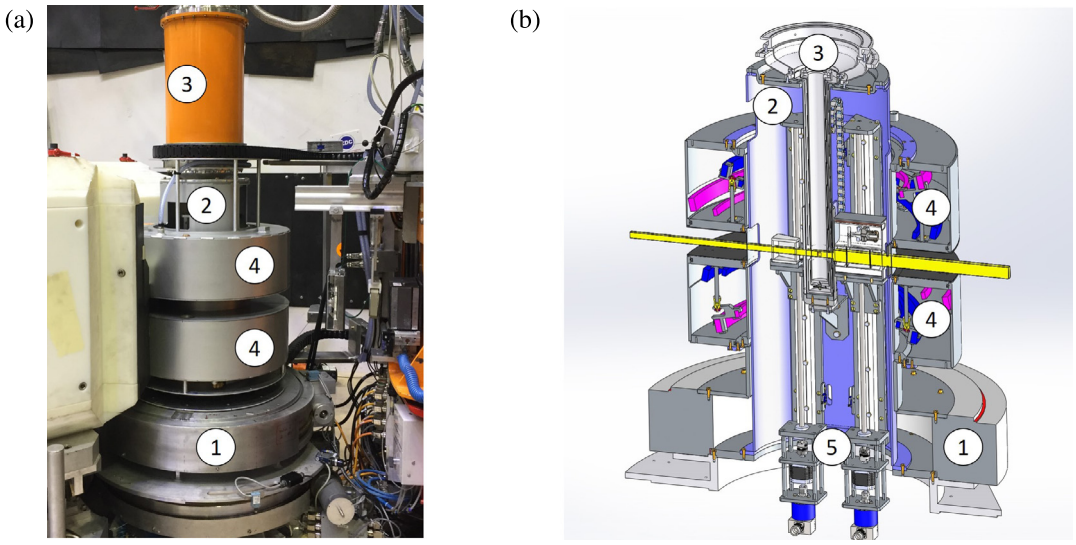


**Fig. 9.** Installation of PASTIS-3 (a) on the IN20 sample table (1). The central part (2), holding the cryostat (3) and the cells, is fixed at the bottom of the table. The magnetic device with the water-cooled cassettes (4) can rotate around the static part (2). (b) Mechanical drawing (sectional view) of the device with the 2 translation stages (5) used to exchange the polarized $^3$He cells and to measure the neutron transmission in both cells independently.

relaxation processes in $^3$He NSF "banana" analyzer cells. In-situ on the spectrometer, the overall polarizer/analyzer relaxation constants are of the order of 100 h. This allows to use PASTIS-3 in real experiments and it will become available as standard equipment in the near future.

## CRediT authorship contribution statement

**David Jullien:** Conceived of the presented idea, Supervision, Analytic calculations, Numerical simulations, Optimization, Computations, Writing - original draft, Discussed the results and contributed to the final manuscript, Experiment tests, Developed the theory in Appendix A, Designed the 3D mechanical models. **Alexandre Petoukhov:** Analytic calculations, Numerical simulations, Optimization, Computations, Writing - original draft, Discussed the results and contributed to the final manuscript, Developed the theory in Appendix A. **Mechthild Enderle:** Writing - original draft, Discussed the results and contributed to the final manuscript, Experiment tests, Found the budgets for the project. **Nicolas Thiery:** Participated in the technical aspects of the experiment, Designed the 3D mechanical models, Realized the mechanical assemblies and built the coils. **Pascal Mouveau:** Participated in the technical aspects of the experiment, Designed the 3D mechanical models. **Ursula Bengaard Hansen:** Experiment tests. **Philippe Chevalier:** Participated in the technical aspects of the experiment. **Pierre Courtois:** Found the budgets for the project.

## Declaration of competing interest

The authors declare that they have no known competing financial interests or personal relationships that could have appeared to influence the work reported in this paper.

## Acknowledgments

We are grateful to Marie Bernadette Lepetit and to Thiery Bigault for discussions, particularly on Appendix. We also would like to thank the technical groups at ILL, which were involved in the construction of the setup.

## Appendix. Magnetic relaxation of a spin-polarized gas from field mapping with an arbitrary orientation of the magnetic probe and robot with respect to the magnetic field.

For the main component of the magnetic field directed along the $Z$-axis, and small gradients of arbitrary form [25] the magnetic relaxation rate of polarized gas confined within a vessel of volume V reads:

$$\Gamma_m = D\left\langle \frac{\|\nabla B_x(\boldsymbol{x})\|^2 + \|\nabla B_y(\boldsymbol{x})\|^2}{\|\boldsymbol{B}(\boldsymbol{x})\|^2} \right\rangle_V \tag{A.1}$$

where D is the gas self-diffusion coefficient, the term in $\langle\rangle_v$ is the field relative gradient in point $\mathbf{x} = \{x,y,z\}$ and the averaging is performed over the vessel volume V.

Let a vector field **B(x)** exists in each point of the 3-D vector space **x** spanned with the orthonormal basis $\mathbf{e}_i$, i = 1, 2, 3:

$$\boldsymbol{x} = \begin{pmatrix} x^1 \\ x^2 \\ x^3 \end{pmatrix} = \sum_{i=1,2,3} x^i \boldsymbol{e}_i \tag{A.2}$$

The vector field **B(x)** is mapped using a 3-component magnetic probe with an arbitrary orientation:

$$\boldsymbol{B}(\boldsymbol{x}) = \begin{pmatrix} B^1(\boldsymbol{x}) \\ B^2(\boldsymbol{x}) \\ B^3(\boldsymbol{x}) \end{pmatrix} = \sum_{i=1,2,3} B^i(\boldsymbol{x})\,\boldsymbol{u}_i \tag{A.3}$$

Here the components $B^i(\mathbf{x})$ are the field readings in the orthonormal probe basis $\mathbf{u}_i$, i = 1, 2, 3. For two points $\mathbf{x}+\boldsymbol{\delta}/2$ and $\mathbf{x}-\boldsymbol{\delta}/2$ separated by a small displacement vector $\boldsymbol{\delta}$ in the vector space **x**:

$$\boldsymbol{\delta} = \begin{pmatrix} \delta^1 \\ \delta^2 \\ \delta^3 \end{pmatrix} = \sum_{i=1,2,3} \delta^i \boldsymbol{e}_i \tag{A.4}$$

we may introduce the vector $\mathbf{D}_{\boldsymbol{\delta}}\mathbf{B(x)}$ representing the variation of the vector **B(x)** along the vector $\boldsymbol{\delta}$:

$$\boldsymbol{D}_{\delta}\boldsymbol{B}(\boldsymbol{x}) = \boldsymbol{B}\left(\boldsymbol{x} + \frac{\boldsymbol{\delta}}{2}\right) - \boldsymbol{B}\left(\boldsymbol{x} - \frac{\boldsymbol{\delta}}{2}\right) \approx (\boldsymbol{\delta}\cdot\nabla)\,\boldsymbol{B}(\boldsymbol{x})$$

$$= \begin{pmatrix} \frac{\partial B^1(\boldsymbol{x})}{\partial x_1}\delta^1 + \frac{\partial B^1(\boldsymbol{x})}{\partial x_2}\delta^2 + \frac{\partial B^1(\boldsymbol{x})}{\partial x_3}\delta^3 \\ \frac{\partial B^2(\boldsymbol{x})}{\partial x_1}\delta^1 + \frac{\partial B^2(\boldsymbol{x})}{\partial x_2}\delta^2 + \frac{\partial B^2(\boldsymbol{x})}{\partial x_3}\delta^3 \\ \frac{\partial B^3(\boldsymbol{x})}{\partial x_1}\delta^1 + \frac{\partial B^3(\boldsymbol{x})}{\partial x_2}\delta^2 + \frac{\partial B^3(\boldsymbol{x})}{\partial x_3}\delta^3 \end{pmatrix} \tag{A.5}$$

Consider the cross product of the field vector $\mathbf{B}\left(\mathbf{x} - \frac{\delta^i}{2}\mathbf{e}_i\right)$ and the field vector $\mathbf{B}\left(\mathbf{x} + \frac{\delta^i}{2}\mathbf{e}_i\right)$ in two points separated by a small displacement $\delta^i$ along the direction $\mathbf{e}_i$.

$$\begin{aligned} &\boldsymbol{B}\left(\boldsymbol{x} - \frac{\delta^i}{2}\boldsymbol{e}_i\right) \times \boldsymbol{B}\left(\boldsymbol{x} + \frac{\delta^i}{2}\boldsymbol{e}_i\right) \\ &\approx \left(\boldsymbol{B}(\boldsymbol{x}) - \frac{\delta^i}{2}\left(\boldsymbol{e}_i \cdot \boldsymbol{\nabla}\right)\boldsymbol{B}(\boldsymbol{x})\right) \times \left(\boldsymbol{B}(\boldsymbol{x}) + \frac{\delta^i}{2}\left(\boldsymbol{e}_i \cdot \boldsymbol{\nabla}\right)\boldsymbol{B}(\boldsymbol{x})\right) \\ &\approx \boldsymbol{B}(\boldsymbol{x}) \times \delta^i \left(\boldsymbol{\nabla}\right)_i \boldsymbol{B}(\boldsymbol{x}) \end{aligned} \tag{A.6}$$

If the vector field **B(x)** at **x**, is directed along the probe component $\mathbf{u}_3$: we have **B(x)** ≈ {0, 0, B(**x**)} and

$$\boldsymbol{B}(\boldsymbol{x}) \times \delta^i \left(\boldsymbol{\nabla}\right)_i \boldsymbol{B}(\boldsymbol{x}) = \delta^i \begin{pmatrix} 0 \\ 0 \\ B(\boldsymbol{x}) \end{pmatrix} \times \begin{pmatrix} \frac{\partial B^1(\boldsymbol{x})}{\partial x_i} \\ \frac{\partial B^2(\boldsymbol{x})}{\partial x_i} \\ \frac{\partial B^3(\boldsymbol{x})}{\partial x_i} \end{pmatrix} = B(\boldsymbol{x})\,\delta^i \begin{pmatrix} -\frac{\partial B^2(\boldsymbol{x})}{\partial x_i} \\ \frac{\partial B^1(\boldsymbol{x})}{\partial x_i} \\ 0 \end{pmatrix} \tag{A.7}$$

Hence, for a probe that has the component $\mathbf{u}_3$ oriented along the main field:

$$\left\| \boldsymbol{B}\left(\boldsymbol{x} - \frac{\delta^i}{2}\boldsymbol{e}_i\right) \times \boldsymbol{B}\left(\boldsymbol{x} + \frac{\delta^i}{2}\boldsymbol{e}_i\right) \right\|^2 \approx \left(\delta^i B(\boldsymbol{x})\right)^2 \left( \left(\frac{\partial B^1(\boldsymbol{x})}{\partial x_i}\right)^2 + \left(\frac{\partial B^2(\boldsymbol{x})}{\partial x_i}\right)^2 \right) \tag{A.8}$$

The same norm may also be written as follows:

$$\left\| \boldsymbol{B}\left(\boldsymbol{x} - \frac{\delta^i}{2}\boldsymbol{e}_i\right) \times \boldsymbol{B}\left(\boldsymbol{x} + \frac{\delta^i}{2}\boldsymbol{e}_i\right) \right\|^2 \approx \left(B(\boldsymbol{x})^2 \sin\theta_i\right)^2 \tag{A.9}$$

where $\theta_i$ is the angle between the vector $\mathbf{B}\left(\mathbf{x} - \frac{\delta^i}{2}\mathbf{e}_i\right)$ and the vector $\mathbf{B}\left(\mathbf{x} + \frac{\delta^i}{2}\mathbf{e}_i\right)$.

From (A.8) and (A.9) follows:

$$\left(\delta^i B(\boldsymbol{x})\right)^2 \left( \left(\frac{\partial B^1(\boldsymbol{x})}{\partial x_i}\right)^2 + \left(\frac{\partial B^2(\boldsymbol{x})}{\partial x_i}\right)^2 \right) \approx \left(B(\boldsymbol{x})^2 \sin\theta_i\right)^2 \tag{A.10}$$

Using (A.10) we build a quadratic form:

$$\begin{aligned} \sum_i \left( \left(\frac{\partial B^1(\boldsymbol{x})}{\partial x_i}\right)^2 + \left(\frac{\partial B^2(\boldsymbol{x})}{\partial x_i}\right)^2 \right) &\approx B(\boldsymbol{x})^2 \sum_i \left(\frac{\sin\theta_i}{\delta^i}\right)^2 \\ &\approx \frac{(B(\boldsymbol{x}))^2}{\delta^2} \sum_i {\theta_i}^2, \quad i = 1,2,3 \end{aligned} \tag{A.11}$$

In the last step in (A.11) we assume a small non-uniformity of the field **B(x)** and the same magnitude of the small displacement in each direction, ($\delta_1 = \delta_2 = \delta_3$). Comparison of the left hand side of (A.11) with the right hand side of (A.1) allows to write:

$$\Gamma_m = \frac{D}{\delta^2}\left\langle \sum_i {\theta_i}^2 \right\rangle_V, \qquad i = 1,2,3 \tag{A.12}$$

The three angles $\{\theta_i\}$, i = 1, 2, 3 required to estimate the magnetic relaxation rate (A.12) from field mapping may be found from:

$$\theta_i = acos \frac{\boldsymbol{B}\left(\boldsymbol{x} - \frac{\delta}{2}\boldsymbol{v}_i\right) \cdot \boldsymbol{B}\left(\boldsymbol{x} + \frac{\delta}{2}\boldsymbol{v}_i\right)}{\left\|\boldsymbol{B}\left(\boldsymbol{x} - \frac{\delta}{2}\boldsymbol{v}_i\right)\right\| \left\|\boldsymbol{B}\left(\boldsymbol{x} + \frac{\delta}{2}\boldsymbol{v}_i\right)\right\|}, \qquad i = 1,2,3 \tag{A.13}$$

Here $\{\mathbf{v}_i\}$ is an arbitrary orthonormal basis.

At this point we note that the sum $\sum_i {\theta_i}^2, i = 1,2,3$ is independent of the basis $\{\mathbf{e}_i\}$ or the orientation of the robot, see (A.2) and (A.4).

No assumptions were made in the choice of $\{\mathbf{e}_i\}$. The same is valid for the left-hand side of (A.11). In addition, the sum $\sum_i {\theta_i}^2, i = 1,2,3$ is also independent of the basis $\{\mathbf{u}_i\}$, since the angles $\{\theta_i\}$ are angles between two vectors. The scalar product as well as the cross product of two vectors are the same for any orthonormal basis. Therefore, in contrast to (A.1), our result (A.12) is valid not only for any orientation of the robot, but also for any orientation of the magnetic probe.

## References


[1] O. Schärpf, H. Capellmann, The XYZ-difference method with polarized neutrons and the separation of coherent, spin incoherent, and magnetic scattering cross sections in a multidetector, Phys. Status Solidi A 135 (1993) 359–379.

[2] J.R. Stewart, P.P. Deen, K.H. Andersen, H. Schober, J.-F. Barthélémy, J.M. Hillier, A.P. Murani, T. Hayes, B. Lindenau, Disordered materials studied using neutron polarization analysis on the multi-detector spectrometer, D7, J. Appl. Cryst. 42 (2009) 69–84.

[3] J.R. Stewart, K.H. Andersen, E. Babcock, C.D. Frost, A. Hiess, D. Jullien, J.A. Stride, J.-F. Barthélémy, F. Marchal, A.P. Murani, H. Mutka, H. Schober, PASTIS: An insert for polarization analysis studies on a thermal inelastic spectrometer, Physica B 385–386 (2006) 1142–1145.

[4] K.H. Andersen, R. Chung, V. Guillard, H. Humblot, D. Jullien, E. Lelièvre-Berna, A. Petoukhov, F. Tasset, First results from Tyrex, the new polarized-3He filling station at ILL, Physica B 356 (2005) 103–108.

[5] G.D. Cates, S.R. Schaefer, W. Happer, Relaxation of spins due to field inhomogeneities in gaseous samples at low magnetic fields and low pressures, Phys. Rev. A 37 (1988) 2877–2885.

[6] K.H. Andersen, D. Jullien, A.K. Petoukhov, P. Mouveau, F. Bordenave, F. Thomas, E. Babcock, Polarized 3He spin-filters using MEOP for wide-angle polarization analysis, Physica B 404 (2009) 2652–2654.

[7] A. Abragam, The Principles of Nuclear Magnetism, Clarendon Press, 1961.

[8] A.N. Bazhenov, V.M. Lobashev, A.N. Pirozhkov, V.N. Slusar, An adiabatic resonance spin-flipper for thermal and cold neutrons, Nucl. Instrum. Methods Phys. Res. A 332 (1993) 534–536.

[9] E. Babcock, A. Petoukhov, J. Chastagnier, D. Jullien, E. Lelièvre-Berna, K.H. Andersen, R. Georgii, S. Masalovich, S. Boag, C.D. Frost, S.R. Parnell, AFP flipper devices: Polarized 3He spin flipper and shorter wavelength neutron flipper, Physica B 397 (2007) 172–175.

[10] M. Enderle, D. Jullien, A. Petoukhov, P. Mouveau, K. Andersen, P. Courtois, PASTIS2 and CROCODILE: XYZ-wide angle polarisation analysis for thermal neutrons, J. Phys.: Conf. Ser. 862 (2017) 012005.

[11] M. Kempa, B. Janousova, J. Saroun, P. Flores, M. Boehm, F. Demmel, J. Kulda, The FlatCone multianalyzer setup for ILL's three-axis spectrometers, Physica B 385–386 (2006) 1080–1082.

[12] W.C. Chen, T.R. Gentile, Q. Ye, A. Kirchhoff, S.M. Watson, J.A. Rodriguez-Rivera, Y. Qiu, C. Broholm, Recent advancements of wide-angle polarization analysis with3He neutron spin filters, J. Phys.: Conf. Ser. 746 (2016) 012016.

[13] Z. Salhi, E. Babcock, R. Gainov, K. Bussmann, H. Kaemmerling, P. Pistel, M. Russina, A. Ioffe, First result from the magic-PASTIS using large 3He SEOP-polarized GE180 doughnut cell, J. Phys.: Conf. Ser. 711 (2016) 012013.

[14] C.J. Beecham, S. Boag, C.D. Frost, T.J. McKetterick, J.R. Stewart, K.H. Andersen, P.M. Bentley, D. Jullien, 3He polarization for ISIS TS2 phase I instruments, Physica B 406 (2011) 2429–2432.

[15] I.A. Zaliznyak, A.T. Savici, V.O. Garlea, B. Winn, U. Filges, J. Schneeloch, J.M. Tranquada, G. Gu, A. Wang, C. Petrovic, Polarized neutron scattering on HYSPEC: the HYbrid SPECtrometer at SNS, J. Phys.: Conf. Ser. 862 (2017) 012030.

[16] C.J. Carlile, et al., Technical Design Report for the European Spallation Source, European Spallation Source, 2013.

[17] E. Babcock, Z. Salhi, R. Gainov, R. Woracek, H. Soltner, P. Pistel, F. Beule, K. Bussmann, A. Heynen, H. Kämmerling, F. Suxdorf, M. Strobl, M. Russina, J. Voigt, A. Ioffe, Recent on-beam tests of wide angle neutron polarization analysis with a 3He spin filter: Magic PASTIS on V20 at HZB, J. Phys.: Conf. Ser. 862 (2017) 012002.

[18] N.R. Newbury, A.S. Barton, G.D. Cates, W. Happer, H. Middleton, Gaseous 3He-3He magnetic dipolar spin relaxation, Phys. Rev. A 48 (1993) 4411–4420.

[19] W.A. Fitzsimmons, L.L. Tankersley, G.K. Walters, Nature of surface-induced nuclear-spin relaxation of gaseous 3He, Phys. Rev. 179 (1969) 156–165.

[20] J. Schmiedeskamp, W. Heil, E.W. Otten, R.K. Kremer, A. Simon, J. Zimmer, Paramagnetic relaxation of spin polarized 3He at bare glass surfaces, Eur. Phys. J. D 38 (2006) 427–438.

[21] A. Deninger, W. Heil, E.W. Otten, M. Wolf, R.K. Kremer, A. Simon, Paramagnetic relaxation of spin polarized 3He at coated glass walls, Eur. Phys. J. D 38 (2006) 439–443.

[22] J. Schmiedeskamp, H.-J. Elmers, W. Heil, E.W. Otten, Yu. Sobolev, W. Kilian, H. Rinneberg, T. Sander-Thömmes, F. Seifert, J. Zimmer, Relaxation of spin polarized 3He by magnetized ferromagnetic contaminants, Eur. Phys. J. D 38 (2006) 445–454.

[23] L.D. Schearer, G.K. Walters, Nuclear spin-lattice relaxation in the presence of magnetic-field gradients, Phys. Rev. 139 (1965) A1398–A1402.

[24] R.L. Gamblin, T.R. Carver, Polarization and relaxation processes in 3He gas, Phys. Rev. 138 (1965) A946–A960.
[25] M. Guigue, G. Pignol, R. Golub, A.K. Petukhov, Universality of spin relaxation for spin-1/2 particles diffusing over magnetic-field inhomogeneities in the adiabatic regime, Phys. Rev. A 90 (2014) 013407.
[26] J.J. Hurly, M.R. Moldover, Ab initio values of the thermophysical properties of helium as standards, J. Res. Natl. Inst. Stand. Technol. 105 (2000) 667.
[27] Q. Ye, T.R. Gentile, J. Anderson, C. Broholm, W.C. Chen, Z. DeLand, R.W. Erwin, C.B. Fu, J. Fuller, A. Kirchhoff, J.A. Rodriguez-Rivera, V. Thampy, T.G. Walker, S. Watson, Wide angle polarization analysis with neutron spin filters, Physics Procedia 42 (2013) 206–212.
[28] A.K. Petoukhov, K.H. Andersen, D. Jullien, E. Babcock, J. Chastagnier, R. Chung, H. Humblot, E. Lelièvre-Berna, F. Tasset, F. Radu, M. Wolff, H. Zabel, Recent advances in polarised 3He spin filters at the ILL, Physica B 385–386 (2006) 1146–1148.
[29] D.I. Meyer, R. Flasck, A new configuration for a dipole magnet for use in high energy physics applications, Nucl. Instrum. Methods 80 (1970) 339–341.
[30] C.L. Goodzeit, M.J. Ball, R. Meinke, The double-helix dipole - A novel approach to accelerator magnet design, IEEE Trans. Appl. Supercond. 13 (2003) 1365–1368.
[31] E.-K. Jeong, D.-H. Kim, M.-J. Kim, S.-H. Lee, J.-S. Suh, Y.-K. Kwon, A solenoid-like coil producing transverse RF fields for MR imaging, J. Magn. Reson. 127 (1997) 73–79.
[32] O. Chubar, P. Elleaume, J. Chavanne, A three-dimensional magnetostatics computer code for insertion devices, J. Synchrotron Radiat. 5 (1998) 481–484.
[33] https://www.wolfram.com/mathematica.
[34] K. Price, R.M. Storn, J.A. Lampinen, Differential Evolution: A Practical Approach to Global Optimization, Springer-Verlag, Berlin Heidelberg, 2005.
[35] A.K. Petoukhov, V. Guillard, K.H. Andersen, E. Bourgeat-Lami, R. Chung, H. Humblot, D. Jullien, E. Lelievre-Berna, T. Soldner, F. Tasset, M. Thomas, Compact magnetostatic cavity for polarised 3He neutron spin filter cells, Nucl. Instrum. Methods Phys. Res. A 560 (2006) 480–484.